



Tests on seismic and shear performance of RC shear walls under alternating axial tensile and compressive loads

Ya-Bo Ding^{a,e}, Hui Chen^{a,b,*}, Wei-Jian Yi^{a,b}, Zhongguo John Ma^c, Jing-Ming Sun^a, Lei He^d, Yun Zhou^{a,b}

^a College of Civil Engineering, Hunan University, Changsha, China

^b Hunan Provincial Key Lab on Damage Diagnosis for Engineering Structures, Changsha, China

^c Department of Civil and Environmental Engineering, The University of Tennessee Knoxville, TN, USA

^d College of Civil Engineering, Tongji University, Shanghai 200092, China

^e Zhangjiajie College, Zhangjiajie, China

ARTICLE INFO

Keywords:

Shear walls
Cyclic tests
Shear strength
Seismic performance
Alternating axial loads

ABSTRACT

Under strong earthquakes, reinforced concrete (RC) shear walls at the bottom of high-rise buildings may experience an internal force state of alternating tension-shear (-bending) and compression-shear (-bending). In order to clarify the seismic and shear performance of shear walls under alternating axial tensile and compressive loads (referred to as alternating axial loads), cyclic tests on five shear-controlled large-scale RC shear walls were conducted in this study. The tests were conducted with synchronized axial loads and horizontal displacements, and a quantitative analysis of the influence of the alternating axial loads was achieved by setting two control specimens. The crack development, failure modes, load-carrying capacity, deformation capacity, and energy dissipation of the specimens were measured and analyzed. The test results indicate that different axial load cases altered the crack pattern and failure mode. With an increase in the target axial tensile load, both tension- and compression-shear capacities of the specimens under alternating axial loads decreased, with the former experiencing a more significant reduction. In comparison to the tension-shear control specimen, it was observed that the alternating axial loads significantly reduced the displacement ductility of shear walls in the tension-shear state, resulting in substantially lower energy dissipation capacity. In addition, based on the tests in this study and the collected shear wall tests, the shear strength formulas in the current codes ACI 318-19 and JGJ 3-2010, as well as a shear model previously proposed by the authors, were evaluated. Based on the test results, a reduction factor was fitted to account for the effect of alternating axial loads on the compressive-shear capacity of RC walls.

1. Introduction

Reinforced concrete (RC) shear walls are widely utilized in concrete structures and serve as crucial components for resisting seismic and wind loads [1–4]. They are subject to combined axial force, shear, and bending moment. In typical situations, the axial force of shear walls is compression. However, as the building height increases, the bottom wall pier may experience tension under strong earthquake [5,6]. When the coupling ratio of a coupled wall is high, axial tension induced by shear forces of coupling beams in one

* Corresponding author. College of Civil Engineering, Hunan University, Changsha, China.

E-mail address: chenhui@hnu.edu.cn (H. Chen).

bottom wall pier may exceed the axial compressive force generated by gravity loads [5]. In such scenarios, bottom wall piers experience an internal force state of alternating tension-shear-bending and compression-shear-bending (referred to as alternating internal force state) under cyclic seismic loads.

A typical case of RC shear walls failure in tension-shear is the collapse of the 15-story Torre Alto Rio building during the 8.8-magnitude earthquake in Chile on February 27, 2010 [7]. Although the specific reasons for the overall collapse of the building and the severe damage to the first-floor shear walls remain inconclusive [8–11], it can be inferred from the concentrated locations of steel rupture and anchorage failure on one side of the building that the shear walls on that side were in a tension-shear state at failure.

During the same earthquake, the 13-story Plaza del Rio building also suffered severe damage and was partially demolished after the earthquake [7,12,13]. From Fig. 1, it can be observed that under the forward seismic loads, the wall developed numerous evenly distributed horizontal cracks (red), with some of them progressing into diagonal cracks. It is noteworthy that one horizontal crack at the top and one diagonal crack in the middle almost penetrated the entire cross-section of Shear wall 2, indicating that the wall was likely in a tension-shear state under the forward seismic loads. Under the reverse seismic loads, the wall was in a compression-shear state, resulting in numerous diagonal cracks (yellow). It can be inferred that the failure surface is composed of diagonal cracks near the bottom of the wall generated in the compression-shear state and horizontal cracks at the bottom of the wall generated in the tension-shear state. Due to the current lack of experimental and theoretical research on shear failure of RC wall piers under alternating axial loads, its mechanical behaviors and failure mechanism remain unclear.

Numerous shear tests on RC shear walls under axial compression have been conducted [14–23], and some scholars [24–30] have established relevant test databases. Existing compression-shear tests indicate that, in general, shear walls failed in shear exhibit poor ductility and energy dissipation capacity. Their stiffness and strength significantly degrade after reaching peak loads. Concrete strength, axial compressive load value (or axial compression ratio), aspect ratio (or shear span-to-depth ratio), boundary element, and reinforcement ratio are dominating factors on the shear performance of shear walls.

Research on tension-shear tests of RC shear walls is relatively limited. Wang et al. [31], Ren et al. [32], Xie et al. [33], Ji et al. [5,34,35], Nie et al. [6], Yao et al. [36] and Wei et al. [37] have conducted about forty tension-shear tests in recent years. The vast majority of these specimens employed small shear span-to-depth ratios (≤ 2.0) and rectangular sections with boundary columns. The test results indicate that, in general, an increase in the axial tensile load reduces the shear strength and lateral stiffness of shear walls. However, compared to shear walls that experience shear failure under axial compression, their ultimate deformation capacity is significantly improved, displaying much better ductility. In reality, due to the cyclic nature of earthquakes, shear walls that have experienced a tension-shear state will be in a compression-shear state under reverse seismic loads, resulting in the alternating tension-shear and compression-shear state. This condition cannot be reflected in the current tension-shear tests on shear walls.

Currently, only 5 RC walls under alternating axial loads were tested to shear failure by Ren et al. [38] and Huang et al. [39]. The test variable is the target axial tensile load, which is the maximum axial tensile load applied to the specimens during the test. The test results show that boundary longitudinal rebars yielded in the tension-shear state, in which state the specimens exhibited good ductility and energy dissipation capacity. In the compression-shear state, the concrete experienced brittle crushing, leading to the ultimate failure of the specimens. The increase in the target axial tensile load reduced the shear strength of the shear walls in both tension-shear and compression-shear states. However, due to the absence of control specimens under non-alternating axial loads in these tests, the effect of the alternating axial loads could not be quantitatively determined. On the other hand, in the existing tests, no moment was applied to the top of shear wall specimens, which fails to realistically simulate the actual internal force state of bottom wall piers in coupled RC shear walls of high-rise buildings.

In order to understand the influence of alternating axial loads on the seismic and shear performance of RC shear walls, this study conducted cyclic tests on five shear-controlled large-scale RC shear walls. These tests aim to simulate the alternating internal force

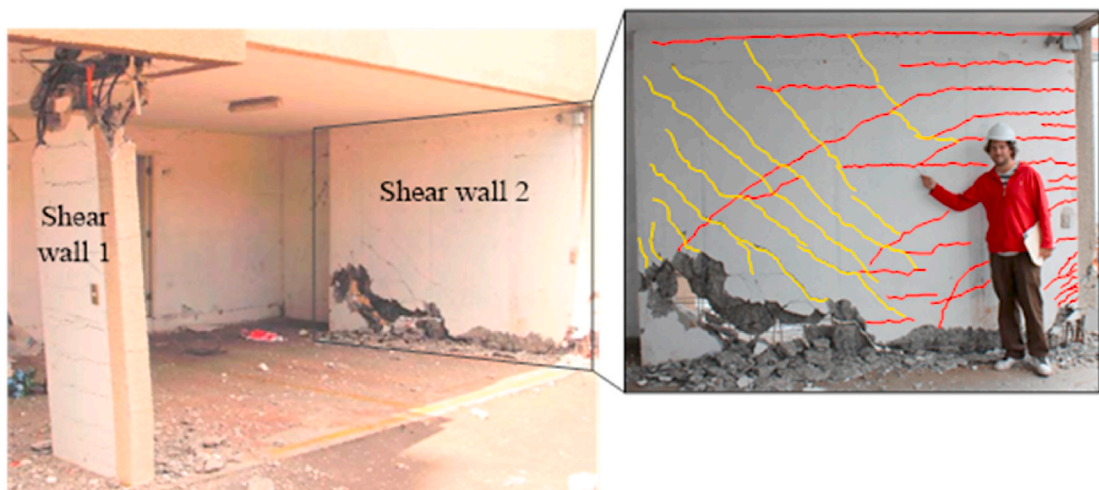


Fig. 1. First-floor shear wall of Plaza del Rio building after 8.8-magnitude earthquake in Chile (adapted from Refs. [7,12]).

state experienced by the bottom wall piers in coupled shear wall structures. Additionally, based on the tests in this study and the collected existing shear wall tests, evaluations and modifications are conducted on the shear strength models for RC shear walls provided by the American code ACI 318-19 [40] and the Chinese code JGJ 3-2010 [41], as well as on a shear model proposed by Ding et al. [42].

2. Experimental program

2.1. Specimen design

In this experiment, five identical shear wall specimens were cast, and their geometric dimensions and reinforcement scheme are shown in Fig. 2. The total height of the specimens was 2.8 m, with the wall portion having a height and length of 1400 mm and a thickness of 150 mm. The longitudinal reinforcement of the boundary columns consisted of 8 ribbed steel rebars with a diameter of 25 mm (D25), and D6 (6 mm diameter) ribbed steel rebars with a 50 mm spacing were used as column stirrups (the stirrup ratio was 0.75 %). It should be noted that the high longitudinal reinforcement ratio was adopted to ensure that the specimens exhibited shear failures. Both horizontal and vertical distributed reinforcement were made of D6 ribbed rebars with a 100 mm spacing (the distributed reinforcement ratios were 0.38 %). The concrete cube compressive strength was designed to be 40 MPa, with the following mix proportions: 360 kg/m³ of 42.5# ordinary Portland cement, 745 kg/m³ of Sand, 180 kg/m³ of water, 1165 kg/m³ of Gravel, with a maximum aggregate size of 20 mm, and a water-to-cement ratio of 0.5.

2.2. Loading program

In this study, five shear wall specimens were subjected to cyclic loading using different loading schemes, simulating the response of

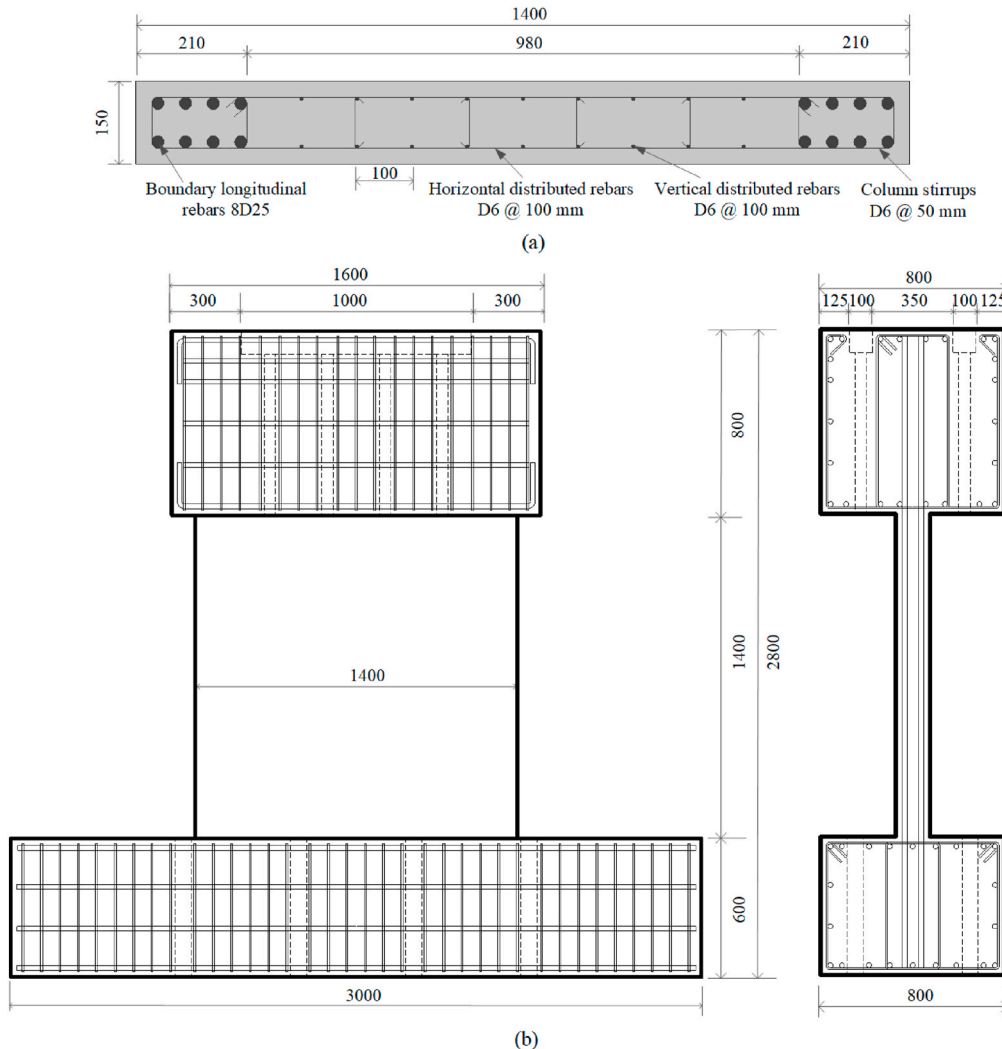


Fig. 2. Reinforcement scheme and geometric dimension (Units: mm) of specimens: (a) wall cross-section; (b) loading and ground beams.

bottom wall piers under alternating axial loads in coupled shear wall structures. The target axial tensile load N_t and target axial compressive load N_c refer to the maximum axial tensile and compressive loads applied to the specimens during the test, respectively. For the specimens under alternating axial loads (Specimens SW10-TC-1/3, SW10-TC-2/3, and SW10-TC-3/3, which are referred to as TC specimens for simplicity), the target axial compressive load was kept constant at 2100 kN, while the target axial tensile load was increased from 700 kN to 2100 kN, as shown in Table 1. The target axial compressive load of 2100 kN corresponded to the maximum axial compression ratio n_c of about 0.3, and the range of the maximum nominal tensile stress n_t corresponding to the target axial tensile loads was between $0.1f_t$ and $0.3f_t$.

$$n_c = |N_c| / f_c A \quad (1)$$

$$n_t = N_t / f_t (A_c + E_s A_{sv} / E_c) \quad (2)$$

where f_c represents the axial compressive strength of concrete, which was taken as 34 MPa at the design stage; f_t represents the axial tensile strength of concrete, which was taken as 2.8 MPa at the design stage; A_g denotes the gross cross-sectional area of shear walls; A_c and A_{sv} respectively represent the cross-sectional area of concrete and vertical rebars (including the boundary longitudinal bars and the vertical distributed bars); E_c and E_s are the elastic modulus of concrete and steel, respectively.

The notation of the shear wall specimens in Table 1 is explained as follows. "SW10" denotes shear wall with an aspect ratio of 1.0; this is followed by the axial loading condition ("TC" for alternating axial tensile and compressive loads, "C" for axial compressive load, "T" for axial tensile load) and the target axial load values (for the TC specimens, the number before "/" corresponds to the maximum nominal tensile stress n_t , and the number after "/" corresponds to the maximum axial compression ratio n_c ; for the control specimens (SW10-T-1 and SW10-C-3) without alternating axial loads, the number corresponds to either n_t or n_c). For example, the specimen SW10-TC-1/3 refers to the shear wall with an aspect ratio of 1.0 that is subjected to alternating axial loads, having n_t of $1.0f_t$ and n_c of 0.3.

The axial load N in the TC specimens changed with the horizontal displacement Δ as shown in Fig. 3 (a). At the initial position of the specimens, the horizontal displacement was zero, and an initial axial compressive load N_g representing the gravity loads was applied. When horizontal displacement was applied, the axial load N exhibited linear variation until it reached the control displacement Δ_c . After reaching Δ_c , the axial load remained constant at the target value N_t or N_c , while horizontal displacement continued to increase. During unloading of the specimen, the axial force followed the loading path back to N_g , as shown in Fig. 3 (a).

The control specimens SW10-T-1 and SW10-C-3 were subjected to cyclic loading with tension-shear and compression-shear loading conditions, respectively. The axial load N variations of SW10-T-1 and SW10-C-3 are represented by the solid black line and the dashed green line, respectively, in Fig. 3 (b).

Lateral loads were applied using a displacement control method, as illustrated in Fig. 3 (c). Due to the overall integrity of the shear walls, floor slabs, and coupling beams, the lateral displacements of the two wall piers in coupled shear walls are nearly identical under seismic loads. Therefore, when the seismic loads in opposite directions are of similar magnitude, the lateral displacements of one wall pier are also similar in opposite directions. Thus, within the each loading level (comprising two loading cycles), a same maximum lateral displacement (absolute value) was applied in the opposite directions to simulate the internal force state of a wall pier within coupled shear walls under cyclic seismic loads.

As shown in Fig. 3 (c), the increment of horizontal displacement at each loading level before reaching the control displacement Δ_c (or $-\Delta_c$) was 1 mm. When the horizontal displacement reached Δ_c (5 mm), the axial load simultaneously reached the target axial load value. Subsequently, with the axial load maintained at the target value, the displacement increment for each level was increased to 3 mm until the horizontal displacement reached 14 mm. Afterward, the displacement increment for each loading level was further increased to 6 mm until the specimen failed. The control displacement Δ_c was defined as the horizontal displacement where the yielding of the boundary longitudinal reinforcement began, as predicted using a nonlinear finite element method. For the sake of convenient comparison among specimens, Δ_c was set to a uniform and conservative value for all the specimens, namely 5 mm. In this experiment, the loading rate was 5 mm/min, and the unloading rate was 10 mm/min.

Through the comparison of the control specimens and SW10-TC-1/3, the influence of alternating axial tension and compression on the seismic and shear performance of the shear walls could be quantitatively determined. On the other hand, by comparing performances of the TC specimens subjected to different target axial tensile loads, the influence of axial tension magnitude could also be identified.

Table 1

Conditions and parameters for axial loading of specimens.

Specimen No.	Axial loading condition	N_t (kN)	N_c (kN)	N_g (kN)	n_t	n_g	n_c
SW10-C-3	Axial compressive load	–	–2100	–700	–	0.1	0.3
SW10-T-1	Axial tensile load	700	–	–700	$1.0f_t$	0.1	–
SW10-TC-1/3	Alternating axial tensile and compressive loads	700	–2100	–700	$1.0f_t$	0.1	0.3
SW10-TC-2/3		1400	–2100	–350	$2.0f_t$	0.05	0.3
SW10-TC-3/3		2100	–2100	0	$3.0f_t$	0	0.3

Notes: N_t is the target axial tensile load; N_c is the target axial compressive load; N_g is the initial axial compressive load; n_t is the maximum nominal tensile stress; n_g is the initial axial compression ratio; n_c is the maximum axial compression ratio.

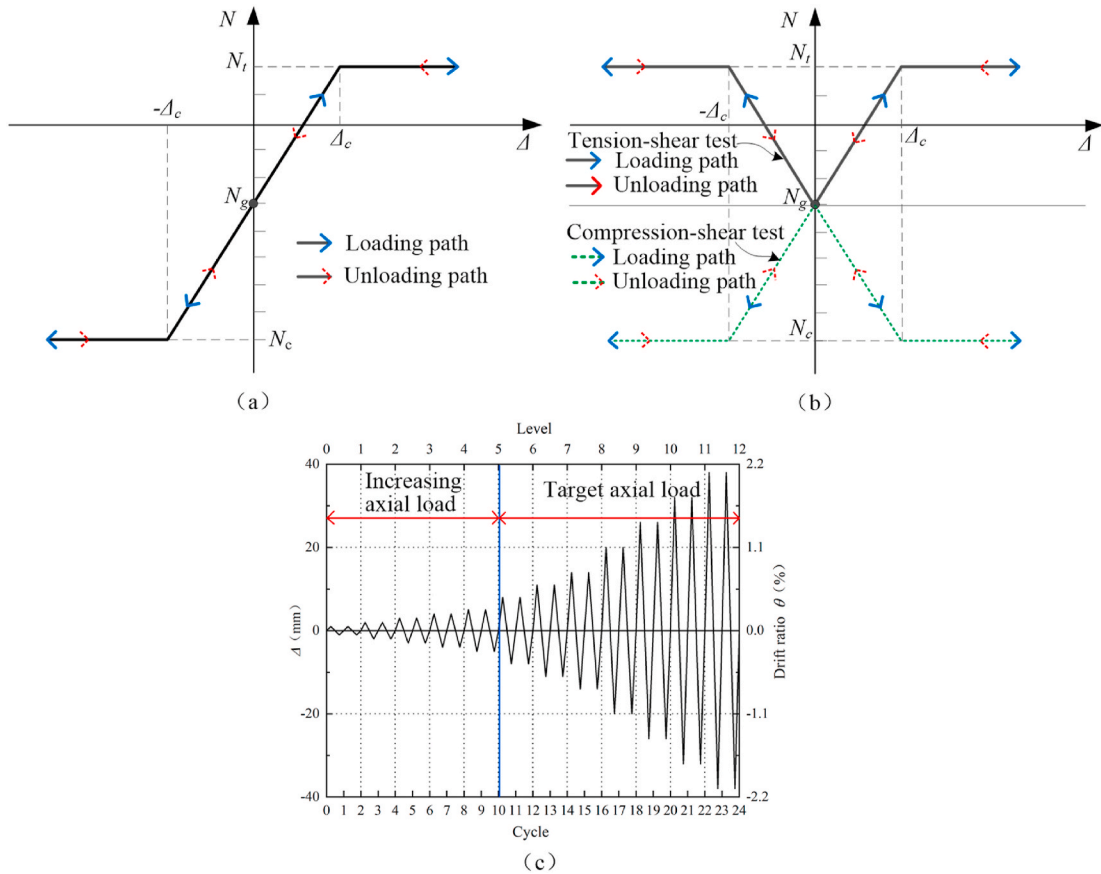


Fig. 3. Loading program: (a) axial loading for TC specimens; (b) axial loading for control specimens; (c) lateral displacements for all specimens.

2.3. Test setup and instrumentation

The test was conducted using the Multi-Usage Structural Testing System (MUST) at Hunan University, as shown in Fig. 4. The MUST enables coordinated vertical and horizontal loading, with a vertical loading capacity of 20,000 kN in compression and 10,000 kN in tension. This is achieved through the synchronization of four vertical actuators, providing a maximum vertical displacement of ± 250 mm. Horizontal loading is controlled by two 2000 kN actuators, offering a maximum loading capacity of ± 4000 kN and a maximum horizontal displacement of ± 400 mm. The rigid loading platform of MUST is positioned 5431 mm above the ground (± 250 mm). To connect with the specimens, which have a height of 2800 mm, a rigid steel-concrete composite platform with a height of 1700 mm and a steel unidirectional hinge were designed and fabricated, as shown in Fig. 4 (a).

In high-rise buildings, bottom wall piers of coupled shear walls not only experience shear and axial forces but also large bending moments. In this test, the axial force and shear force were applied to the specimens through the steel hinge. The shear force was located 1400 mm from the top surface of the wall portion, generating a moment at the top surface, constituting 50 % of the moment at the bottom section of the wall portion. The determination of the ratio of bending moments at the top and bottom surfaces (referred to as bending moment ratio) of the walls in this study was based on nonlinear numerical simulations of a five-story coupled wall specimen CW-2 [43]. The aspect ratio of the bottom wall pier of the coupled wall was 1.17, and the axial compression ratio n_g under the initial axial compressive load was 0.1, which are close to the ratios of the test specimens in this study. Numerical results indicated that the bottom wall pier experienced alternating axial tension and compression under horizontal cyclic loading, with a maximum nominal tensile stress n_t of approximately $1.7f_c$, which falls within the range of n_t studied in this test. The bending moment ratio of the bottom wall pier mostly varied between 0.3 and 0.8. When the wall pier was under compression, the ratio was relatively stable, generally ranging from 0.5 to 0.7. Considering the size limitations of the loading device and the steel hinge, 0.5 was adopted as the bending moment ratio for the test specimens in this study. The applied loading setup allows for a more realistic simulation of the internal force state of bottom wall piers in coupled shear walls.

Fig. 5 shows the arrangement of displacement sensors (LVDTs) and strain gauges. As depicted in Fig. 5 (a), displacement sensors W1 and W2 measured the horizontal displacement at the midpoints of the steel hinge and loading beam, respectively. W3 to W5 measured the horizontal displacement of the wall at different heights, W6 measured the horizontal displacement of the ground beam, W7 and W8 measured the vertical displacement of the loading beam, and W9 and W10 measured the vertical displacement of the ground beam. It is important to note that the applied displacement during the test was controlled by the difference between W2 and W6 ($W2-W6$), which

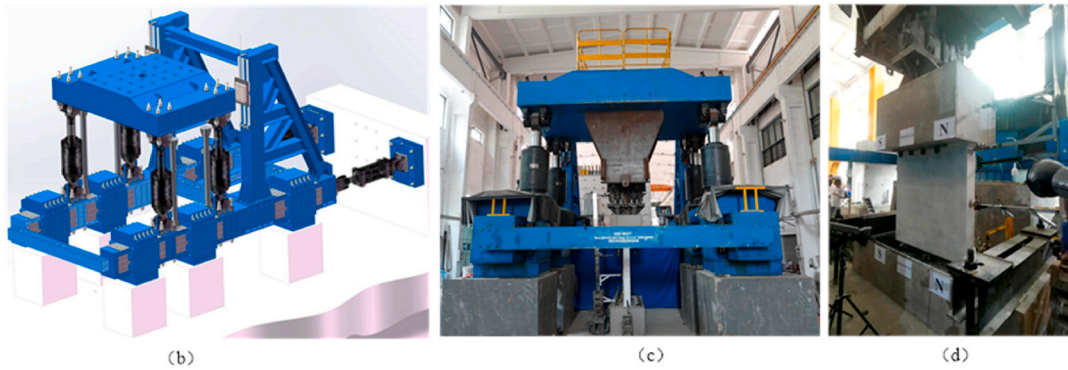
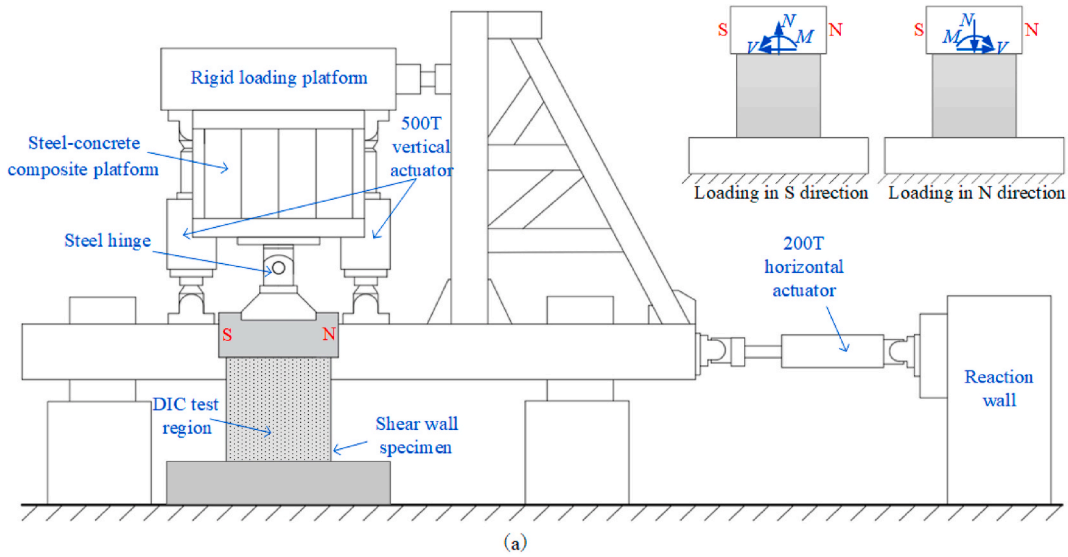


Fig. 4. Test setup: (a) Schematic loading conditions; (b) Schematic MUST system; (c) Photograph of MUST system and Steel-concrete composite platform; (d) Photograph of specimen and steel hinge.

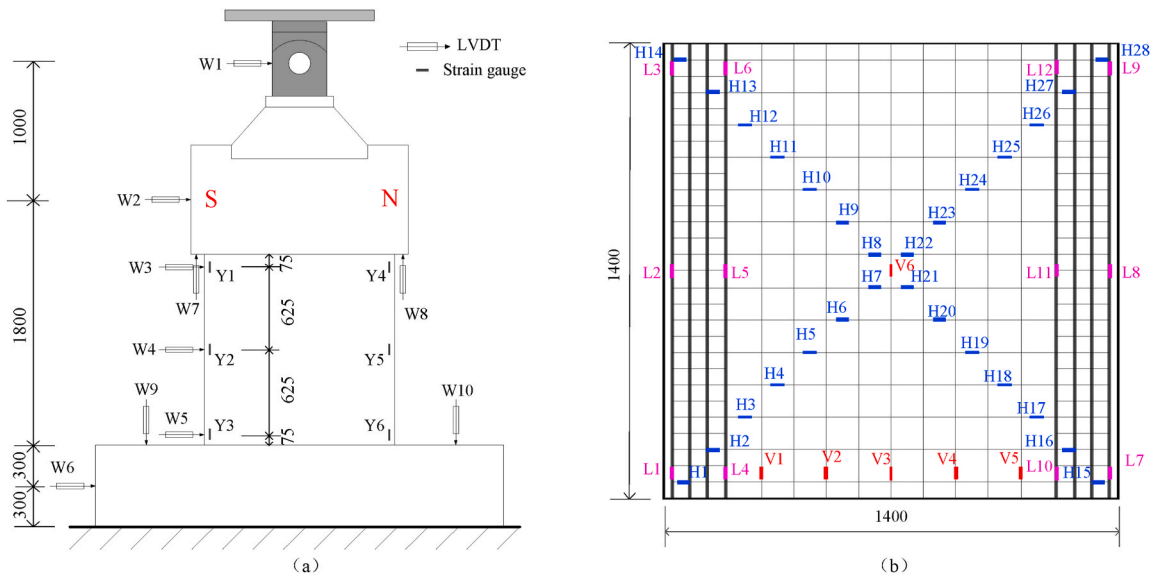


Fig. 5. Layout of instruments: (a) displacement transducers and concrete strain gauges; (b) rebar strain gauges.

is also referred to as the horizontal displacement value of the specimens mentioned in the following text.

The locations of the rebar strain gauges are shown in Fig. 5 (b). Twelve strain gauges (L1 to L12) were used to measure the strains of the boundary longitudinal reinforcement, twenty-eight strain gauges (H1 to H28) were used to measure the strains of the horizontal distributed reinforcement, and six strain gauges (V1 to V6) were used to measure the strains of the vertical distributed reinforcement. The positions of the strain gauges on the horizontal distributed reinforcement were arranged according to the diagonal lines of the wall (anticipated critical shear cracks). Concrete strain gauges were attached to the surface of the wall and were labeled as Y1 to Y6, as shown in Fig. 5 (a).

In order to comprehensively record the deformation and crack development of the wall, a Digital Image Correlation (DIC) based strain measurement system was employed to measure the strain fields of the wall portions during the entire loading process. The system primarily consisted of the VIC-3D software and two Basler industrial cameras (4096*3000 pixels @ 30 fps). As shown in Fig. 4 (a), the DIC test region covered the wall portion (1400 mm × 1400 mm). Due to the obstruction of the vertical screws and nuts under the loading beam (Fig. 4 (d)), the effective DIC test region was approximately 1300 mm in height.

2.4. Material properties

The measured concrete strength for the specimens are shown in Table 2. On the day of the specimen test, six concrete cubes (with a side length of 150 mm) and three concrete cylinders (with a diameter of 150 mm and a height of 300 mm) cured under the same conditions were tested. Their average values (standard deviations) were regarded as the concrete cubic compressive strength f_{cu} ($f_{cu,SD}$) and cylinder compressive strength f_c' (f_c',SD) of the specimen.

The D25, D12, and D6 ribbed steel rebars used in the test are all of HRB400 grade, with diameters of 25 mm, 12 mm, and 6 mm, respectively. Three samples were selected for each type of the rebars for material property testing, and their average values were taken as the measured strength. The measured results of the elastic modulus, yield strength, ultimate strength, and ultimate strain of the rebars are presented in Table 3.

3. Test results

3.1. Crack development and failure characteristics

Shear wall specimens exhibited varied mechanical behaviors under different axial loading conditions. This section describes the crack development during the loading process and failure characteristics of the specimens. Figs. 6 and 7 present the principal tensile strain distributions provided by the VIC-3D software, to represent cracks appearing on the front surface of the wall portions. Higher values of principal tensile strain qualitatively indicate wider cracks at the corresponding locations.

Fig. 6 illustrates the crack patterns of the specimens when the absolute horizontal displacement reached 8 mm in the south (S) and north (N) directions, which were respectively defined as the positive and negative directions for the horizontal displacement. This displacement was close to the yield displacement (see Table 4) of the TC specimens but less than the peak displacement of the specimens (horizontal displacement corresponding to the peak load). The crack patterns of the two control specimens in both S and N directions were relatively symmetrical about the vertical axis of the specimens, as shown in Fig. 6 (a)–(d). However, due to the spatial randomness of concrete strength, cracks cannot be perfectly symmetric even under symmetric axial forces. The crack development in the tension-shear control specimen SW10-T-1 was more pronounced, with larger crack quantities, widths, and lengths compared to the compressive-shear control specimen SW10-C-3.

Notably, the TC specimens subjected to alternating axial loading exhibited significant differences in S and N directions, as depicted in Fig. 6 (e)–(j). In the N direction, the TC specimens were in a compression-shear state, where crack development was to some extent suppressed by the axial compressive force, resulting in relatively fewer and narrower cracks. Conversely, in the S direction, the TC specimens were in a tension-shear state, and the tensile load facilitated crack propagation, leading to a considerable increase in crack quantity, width, and length. Additionally, with the increase in target axial tensile load, the distribution range of diagonal cracks expanded, accompanied by an increase in their width and a decrease in their angle with the horizontal plane.

Fig. 7 illustrates the crack patterns of each shear wall specimen when reaching the peak displacement in the S and N directions. The peak displacements in the S and N directions for the control specimens are close (refer to Table 4). SW10-C-3 first reached the peak shear load in the N direction, as shown in Fig. 7 (b), where a critical shear crack diagonally crossed the wall. At this point, the cracks produced under S direction loading (referred to as cracks in S direction) essentially closed, with only several narrower diagonal cracks visible. Subsequently, when the specimen reached the peak shear load in the S direction, as shown in Fig. 7 (a), besides the newly formed cracks in S direction, the critical shear crack previously generated under the peak shear load in the N direction still maintained a substantial width. This might have caused the slightly lower peak shear load in the S direction compared to that in the N direction for SW10-C-3.

Table 2
Measured concrete strength for specimens.

Specimen No.	f_{cu} (MPa)	$f_{cu,SD}$ (MPa)	f_c' (MPa)	f_c',SD (MPa)
SW10-C-3	36.18	3.28	29.03	2.35
SW10-T-1	44.62	3.77	33.90	1.44
SW10-TC-1/3	44.44	3.13	35.11	2.28
SW10-TC-2/3	43.54	2.58	33.43	1.37
SW10-TC-3/3	41.86	3.85	32.45	2.16

Table 3
Measured values of ribbed steel rebars.

Type	Elastic modulus (MPa)	Yield strength (MPa)	Ultimate strength (MPa)	Ultimate strain
D25	2.12×10^5	425.85	576.49	0.124
D12	2.00×10^5	440.24	665.42	0.137
D6	2.08×10^5	466.28	614.90	0.151

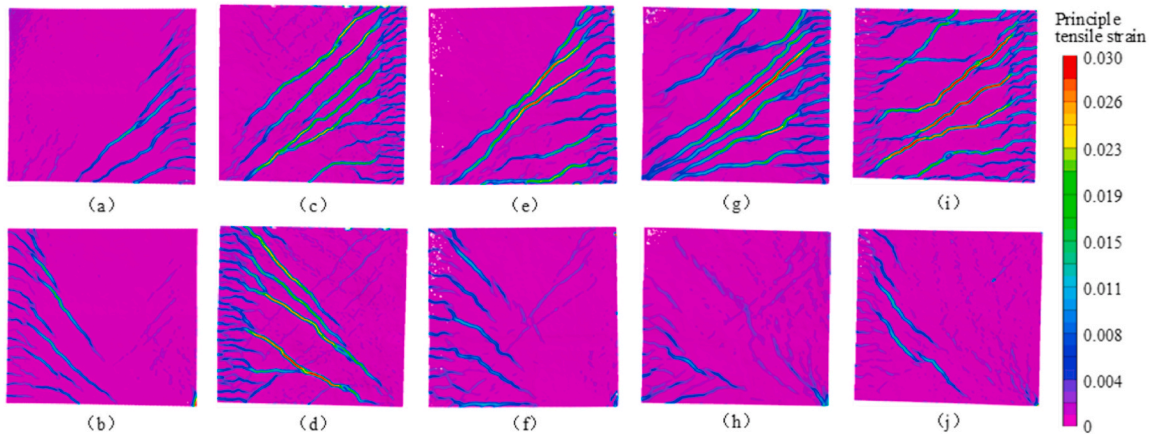


Fig. 6. Crack patterns of the specimens when $\Delta = \pm 8$ mm visualized by DIC technique: (a) SW10-C-3 (S); (b) SW10-C-3 (N); (c) SW10-T-1 (S); (d) SW10-T-1 (N); (e) SW10-TC-1/3 (S); (f) SW10-TC-1/3 (N); (g) SW10-TC-2/3 (S); (h) SW10-TC-2/3 (N); (i) SW10-TC-3/3 (S); (j) SW10-TC-3/3 (N).

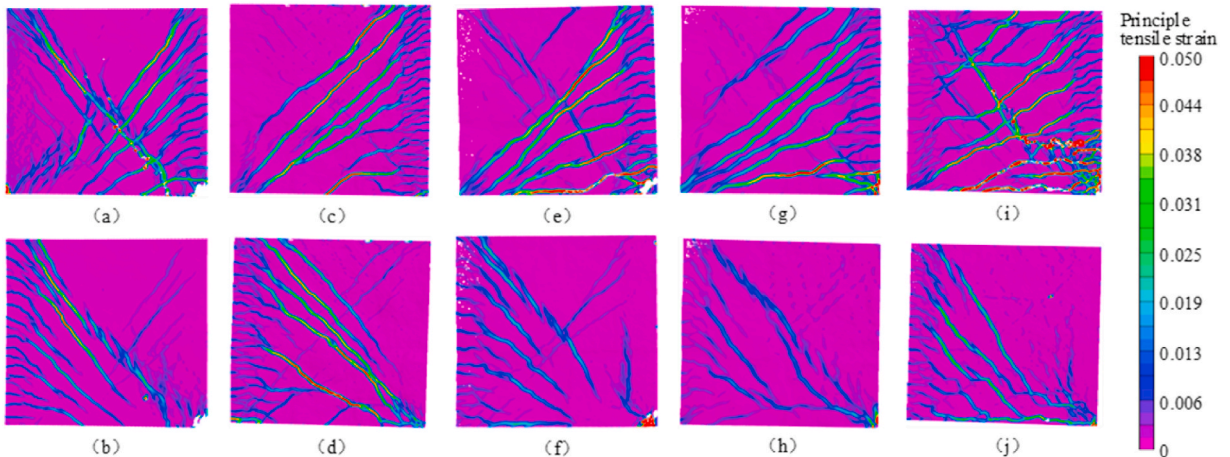


Fig. 7. Crack patterns of the specimens when $\Delta =$ peak displacements visualized by DIC technique: (a) SW10-C-3 (S); (b) SW10-C-3 (N); (c) SW10-T-1 (S); (d) SW10-T-1 (N); (e) SW10-TC-1/3 (S); (f) SW10-TC-1/3 (N); (g) SW10-TC-2/3 (S); (h) SW10-TC-2/3 (N); (i) SW10-TC-3/3 (S); (j) SW10-TC-3/3 (N).

The tension-shear control specimen SW10-T-1 first reached the peak shear load under the S direction loading (Fig. 7 (c)). When it reached the peak shear load in the N direction, the cracks in S direction essentially closed, with only a few narrower diagonal cracks visible (Fig. 8 (d)). The peak shear loads in both directions for this specimen were very close (differing by only about 2 %), and the crack patterns at the positive and negative peak displacements were nearly symmetrical.

As shown in Fig. 7 (e)–(j), the crack patterns of the TC specimens were markedly asymmetric when reaching peak displacements in both directions. These specimens first reached the peak shear load in the N direction (referred to as compression-shear strength), forming a critical shear crack traversing the wall. In the subsequent loading level, the specimens reached the shear peak load in the S direction (referred to as tension-shear strength), typically resulting in multiple diagonal cracks traversing the wall. With an increase in the target axial tensile load N_p , the horizontal (flexural) cracks at the wall bottom of the TC specimens gradually extended and widened under the compression-shear strength, as shown in Fig. 7(f)–(h), and (j). This led to a reduction in the compression zone depth of the shear walls, potentially adversely affecting the shear performance of the specimens under compression. On the other hand, as N_t increased, the angle between the diagonal cracks and the horizontal plane decreased for the TC specimens under the tension-shear

Table 4
Shear capacity and displacement of specimens.

Specimen No.	Direction	Yield displacement (mm)	Yield shear load (kN)	Peak displacement (mm)	Peak shear load (kN)	Ultimate displacement (mm)	Ultimate shear load (kN)	Ductility coefficient
SW10-C-3	S	11.43	821.8	17.7	983	21.33	835.6	1.87
	N	10.63	859	18.1	1010	19.6	882	1.84
SW10-T-1	S	9.47	576.9	14.33	685	38.8	582.2	4.1
	N	8.49	563.9	13.99	676.9	37.9	575.4	4.47
SW10-TC-1/3	S	10.11	560.4	17.16	685.1	20.2	642.6	2.0
	N	8.35	900.4	14.01	1038.6	16.92	882.8	2.02
SW10-TC-2/3	S	7.64	429.3	13.81	512.3	14.21	451.4	1.86
	N	8.06	840	10.94	941.5	13.99	800.3	1.74
SW10-TC-3/3	S	8.36	323.4	17.64	360.4	20.46	348.1	2.45
	N	9.71	786.1	14.09	898.2	15.13	763.5	1.56

Notes: Ductility coefficient $\mu = \Delta_u/\Delta_y$, where Δ_u and Δ_y represent the ultimate displacement and yield displacement, respectively.

strength (Fig. 7(e)–(g), and (i)), leading to fewer horizontal bars intersecting with the diagonal cracks. This may be one of the main reasons for the reduction in the tension-shear strength of RC shear walls as the axial tensile load increases.

Fig. 8 shows post-failure photographs of the specimens. The failure mode of SW10-C-3 is characterized by shear failure, as depicted in Fig. 8 (a), where concrete spalling occurred near the critical shear cracks, predominantly concentrated in the lower part of the cracks. Concrete in the compressed region at the bottom of the wall exhibited crushing. From Fig. 8 (b), it can be observed that SW10-T-1 exhibited sliding failure near the wall bottom. At the point of peak displacement, as shown in Fig. 7 (c) and (d), SW10-T-1 mainly displayed diagonal shear cracks without the formation of a slip failure surface, which developed subsequently under cyclic loading. Hence, this failure mode is termed as shear-sliding failure.

The specimens SW10-TC-1/3 and SW10-TC-2/3 under alternating axial loads exhibited a typical shear failure mode, as depicted in Fig. 8 (c) and (d). Their failure surfaces developed from the critical shear cracks formed under compression-shear, accompanied by concrete spalling near these critical cracks. Moreover, the concrete in the compressed zone at the wall bottom experienced crushing. On the other hand, although the cracks developed more extensively under tension-shear during the loading process (as observed in Figs. 6 and 7), the cracks generated in the tension-shear state essentially closed after final failure. Hence, the post-failure damage state of the TC specimens displayed significant asymmetry, as shown in Fig. 8 (c)–(e).

From Fig. 8 (e), it is evident that the failure surface of specimen SW10-TC-3/3 differs somewhat from specimens SW10-TC-1/3 and SW10-TC-2/3. It comprises critical shear cracks formed under compression-shear and a horizontal crack generated at a certain distance from the bottom surface under tension-shear. By comparing Fig. 7 (j) and 8 (e), it can be observed that the horizontal part of the failure surface formed after the compression-shear strength. Hence, the failure mode of SW10-TC-3/3 could also be considered as shear failure. Notably, the failure surface of SW10-TC-3/3 resembles to the failure surface observed in the practical shear wall post an seismic event, which also displayed a significantly asymmetric damaged state, as depicted in Fig. 1.

3.2. Hysteresis curves

Fig. 9 shows the hysteresis curves of shear load (V) versus the horizontal displacement (Δ) at the midpoints of the loading beam of for each specimen. In the figure, θ represents the lateral drift ratio of the shear walls, which equals Δ divided by the distance from the midpoints of the loading beam to the top surface of the foundation beam. Prior to reaching the peak shear load, the hysteresis curves of the control specimens are symmetric around the coordinate axis origin, whereas those of the TC specimens are asymmetric, indicating significantly different load-carrying and deformation behaviors of the TC specimens in the S and N directions. Specimen SW10-C-3 (Fig. 9 (a)) first reached its peak shear capacity in the N direction, then in the S direction, followed by a rapid decrease in shear strength. The hysteresis curve of specimen SW10-T-1 is plumper, reaching its peak shear load after the yielding of boundary longitudinal rebars, followed by a slow decrease in capacity as depicted in Fig. 9 (b).

As shown in Fig. 9 (c)–(e), the lateral displacement corresponding to the peak shear load in the N direction for the TC specimens is smaller than that for the peak shear load in the S direction, with specific values provided in Table 4. This indicates that these specimens first reached the compression-shear strength and subsequently achieved the tension-shear strength in the next loading level. After reaching the tension-shear strength, the TC specimens experienced a rapid decrease in the shear load-carrying capacity under axial compression, ultimately leading to shear failure (controlled by the crushing of concrete in the compression zone). After that, these specimens could not return to the position with zero lateral displacement while maintaining the corresponding axial load N_g . Therefore, it can be considered that the coupled shear wall structure in which the wall pier is located has been completely damaged, and there is no need for further tension-shear loading.

3.3. Lateral resistance and displacement ductility

Fig. 9 also shows the skeleton curves and characteristic points of each specimen, where the yield characteristic points (yield displacement and yield load) were obtained using the energy equivalence method [44]. The ultimate lateral displacement of the specimens was taken as the smaller value of the displacement when the shear capacity dropped to 85 % of the peak shear load in the descending section of the skeleton curve and the maximum displacement, and the corresponding shear load of the ultimate displacement was defined as the ultimate load. The displacement ductility coefficient μ is the ratio of the ultimate displacement to the

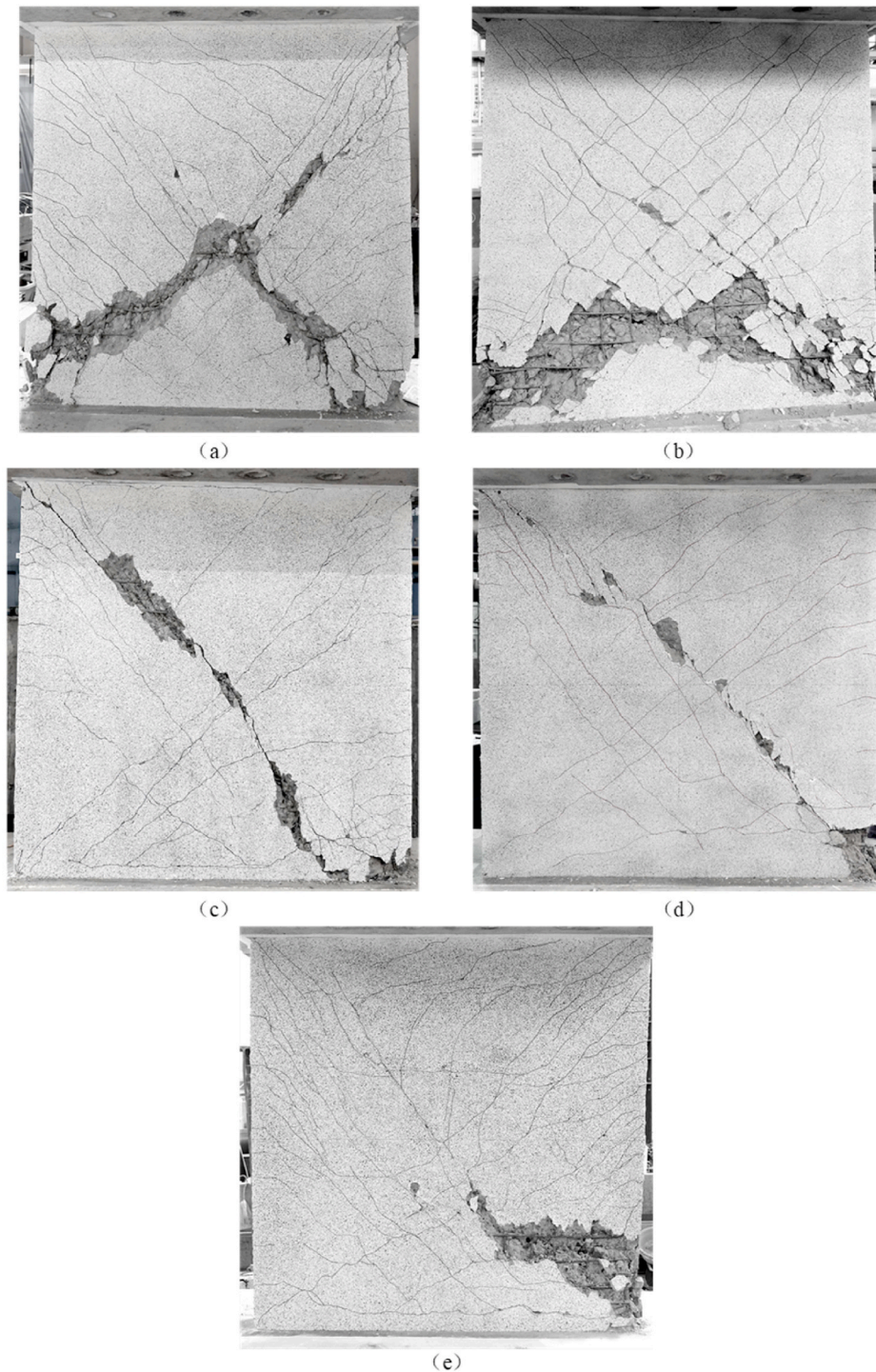


Fig. 8. Post-failure photographs of specimens: (a) SW10-C-3; (b) SW10-T-1; (c) SW10-TC-1/3; (d) SW10-TC-2/3; (e) SW10-TC-3/3.

yield displacement. Table 4 provides the specific values of the characteristic points and ductility coefficient. For the convenience of comparison, the skeleton curves of the specimens were extracted and displayed in Fig. 10.

To eliminate the influence of concrete strength variation on the comparison of shear strength V_t (peak shear load) of the specimens, a quantitative analysis was conducted on the normalized shear strength $V_t/(b_w d_w f_c)$ to assess the effect of alternating axial loads on the lateral resistance of shear walls. Where b_w and d_w are the web thickness and effective height of the wall cross-section, respectively. As shown in Fig. 11 (a), the tension-shear strength of specimen SW10-TC-1/3 was close to the average shear strength of the control

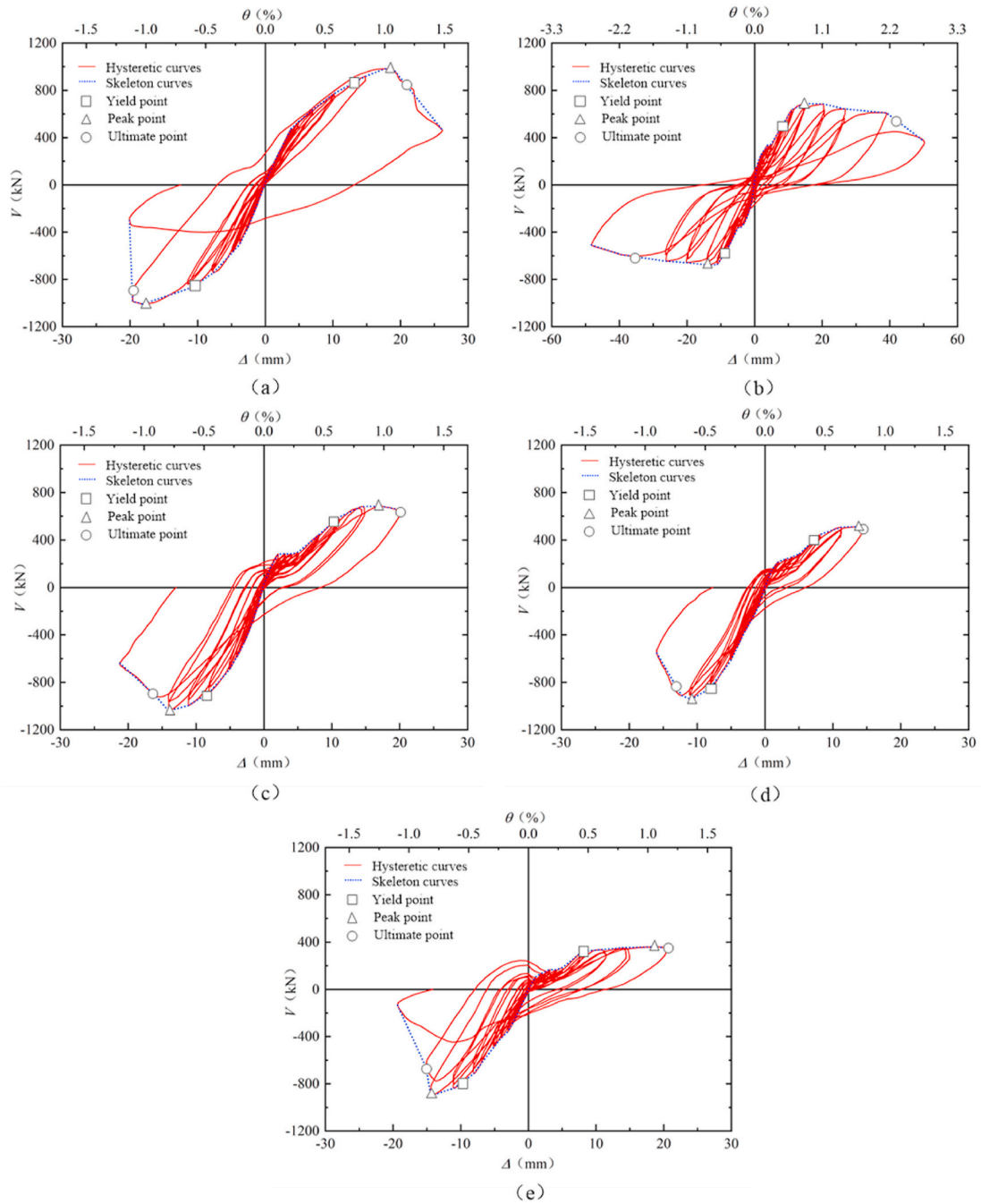


Fig. 9. Hysteresis curves of shear load V versus the horizontal displacement Δ : (a) SW10-C-3; (b) SW10-T-1; (c) SW10-TC-1/3; (d) SW10-TC-2/3; (e) SW10-TC-3/3.

specimen SW10-T-1. With an increase in the target axial tensile load N_t , the tension-shear strength significantly decreased. SW10-TC-2/3 and SW10-TC-3/3 exhibited reductions of 23.7 % and 44.7 %, respectively, compared to SW10-T-1. From Fig. 11 (b), it can be observed that the compression-shear strength of TC specimens decreased to a certain extent compared to the control specimen SW10-C-3. The compression-shear strength of SW10-TC-1/3, SW10-TC-2/3, and SW10-TC-3/3 were reduced by 13.8 %, 18 %, and 19.4 %, respectively, compared to the mean shear strength of SW10-C-3. This indicates that the decrease in tension-shear strength is greater than that in compression-shear strength with an increase in the target axial tensile load.

Fig. 11 (c) and (d) compare the displacement ductility coefficients μ of the specimens. Compared to the control specimen SW10-T-1, the ductility coefficients of SW10-TC-1/3, SW10-TC-2/3, and SW10-TC-3/3 in the tension-shear state decreased by 52.6 %, 56.1 %, and 41.9 %, respectively. This indicates a significant reduction in the displacement ductility performance of the TC specimens in the tension-shear state. The main reason for this result is that after the rapid failure in the compression-shear state, the TC specimens were

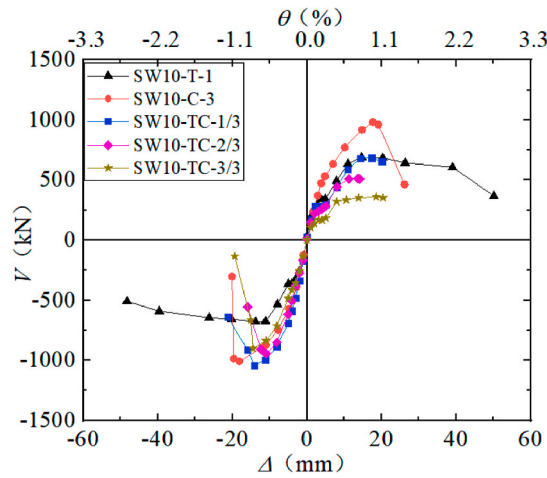


Fig. 10. Skeleton curves of shear load V versus the horizontal displacement Δ

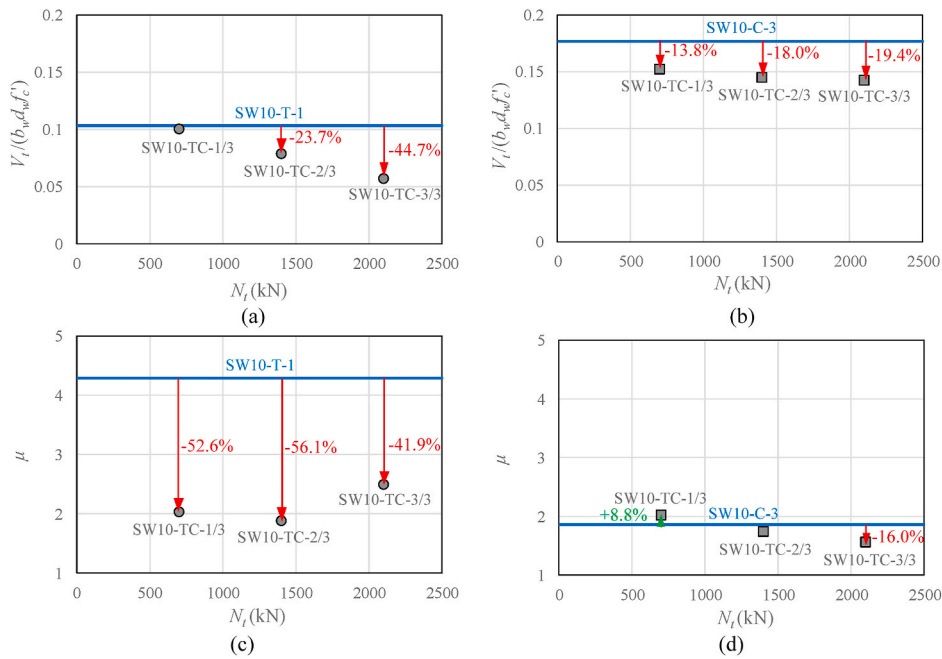


Fig. 11. Comparison of shear strength and displacement ductility of specimens: (a) normalized tension-shear strength; (b) normalized compression-shear strength; (c) displacement ductility coefficients in tension-shear state; (d) displacement ductility coefficients in compression-shear state.

unable to undergo the subsequent tension-shear loading as initially planned, thus unable to exhibit their good ductility performance in the tension-shear state. On the other hand, the alternating axial loads had no significant impact on the ductility performance of the specimens in the compression-shear state.

3.4. Lateral stiffness degradation

The lateral shear stiffness K of each shear wall specimen is depicted in Fig. 12. The lateral shear stiffness K of shear walls at each loading level equals the maximum shear load of that level divided by the corresponding horizontal displacement. It's evident that the stiffnesses K of all the specimens decrease as the lateral displacement increases, and this reduction diminishes gradually. Moreover, with an increase in the target axial tensile load, the lateral stiffnesses of the TC specimens decrease at the same displacement, regardless of being in tension-shear or compression-shear states. The degradation of lateral stiffness is more pronounced in tension-shear than in compression-shear state.

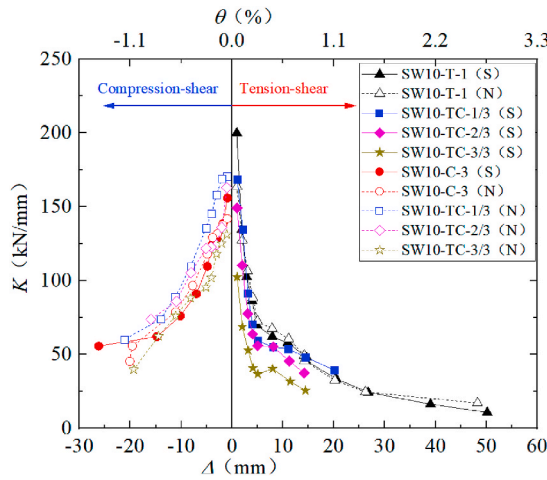


Fig. 12. Degradation of lateral shear stiffness of specimens.

3.5. Energy dissipation capacity

The energy dissipation capacity is a crucial metric for assessing the seismic performance of reinforced concrete shear walls. The accumulated energy consumption E , as depicted in Fig. 13, was determined by computing the area enclosed within the hysteresis loops according to $E = \sum_{i=1}^n \sum_{j=1}^2 S_{ij}$, where S_{ij} represents the area enclosed by the hysteresis loop of the j^{th} cycle at the i^{th} loading level. It's evident that the tension-shear control specimen SW10-T-1 exhibited the highest energy dissipation capacity, significantly outperforming the compression-shear control specimen SW10-C-3. The accumulated energy consumption of the TC specimens were similar to that of SW10-C-3, with SW10-TC-2/3 even lower than that of SW10-C-3. The main reason for this result is the poor displacement ductility performance of the TC specimens, which prevented the specimens from fully utilizing the energy dissipation capacity of RC shear walls in tension-shear state.

3.6. Boundary longitudinal reinforcement strains

Fig. 14 presents measured strains of boundary longitudinal bars for the specimens when reaching the maximum horizontal displacement at each loading level. It's important to note that measurements showing significant anomalies or those obtained from strain gauges damaged during the specimen fabrication have been excluded. From Fig. 14, it shows that for the control specimen SW10-C-3, the longitudinal bars experienced compressive yielding in compression-shear, corresponding to an average absolute value of approximately 10.8 mm for the horizontal displacements in the S and N directions. In contrast, for the control specimen SW10-T-1, the boundary longitudinal bars underwent tensile yielding in tension-shear, corresponding to an average absolute value of approximately 7.4 mm for the horizontal displacements. For the TC specimens SW10-TC-1/3, SW10-TC-2/3, and SW10-TC-3/3 in the tension-shear state, the horizontal displacements at the onset of rebar yielding were 9.8 mm, 5.2 mm, and 4.1 mm, respectively. On the other hand, in the compression-shear state, the horizontal displacements at the onset of rebar yielding were -6.3 mm, -6.9 mm, and -6.3 mm, respectively. This indicates that with an increase in the target axial tensile load, the horizontal displacement of the TC specimens corresponding to longitudinal reinforcement yielding significantly decreased in the tension-shear state, while remaining relatively stable in the compression-shear state. In other words, the axial tensile load accelerated the tensile yielding of the boundary longitudinal bars. For the specimen SW10-TC-1/3 with the lowest target axial tensile load, the longitudinal bars experienced the compressive yielding in the compression-shear state first, followed by the tensile yielding in the tension-shear state. However, for the higher target axial tensile loads, the tensile yielding of the longitudinal bars occurred earlier in the tension-shear state than the compressive yielding in the compression-shear state, as observed in the specimens SW10-TC-2/3 and SW10-TC-3/3. Based on the measured longitudinal

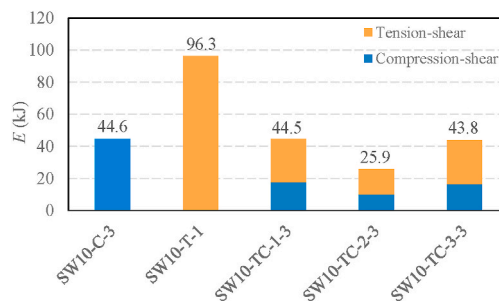


Fig. 13. Accumulated energy consumption of specimens.

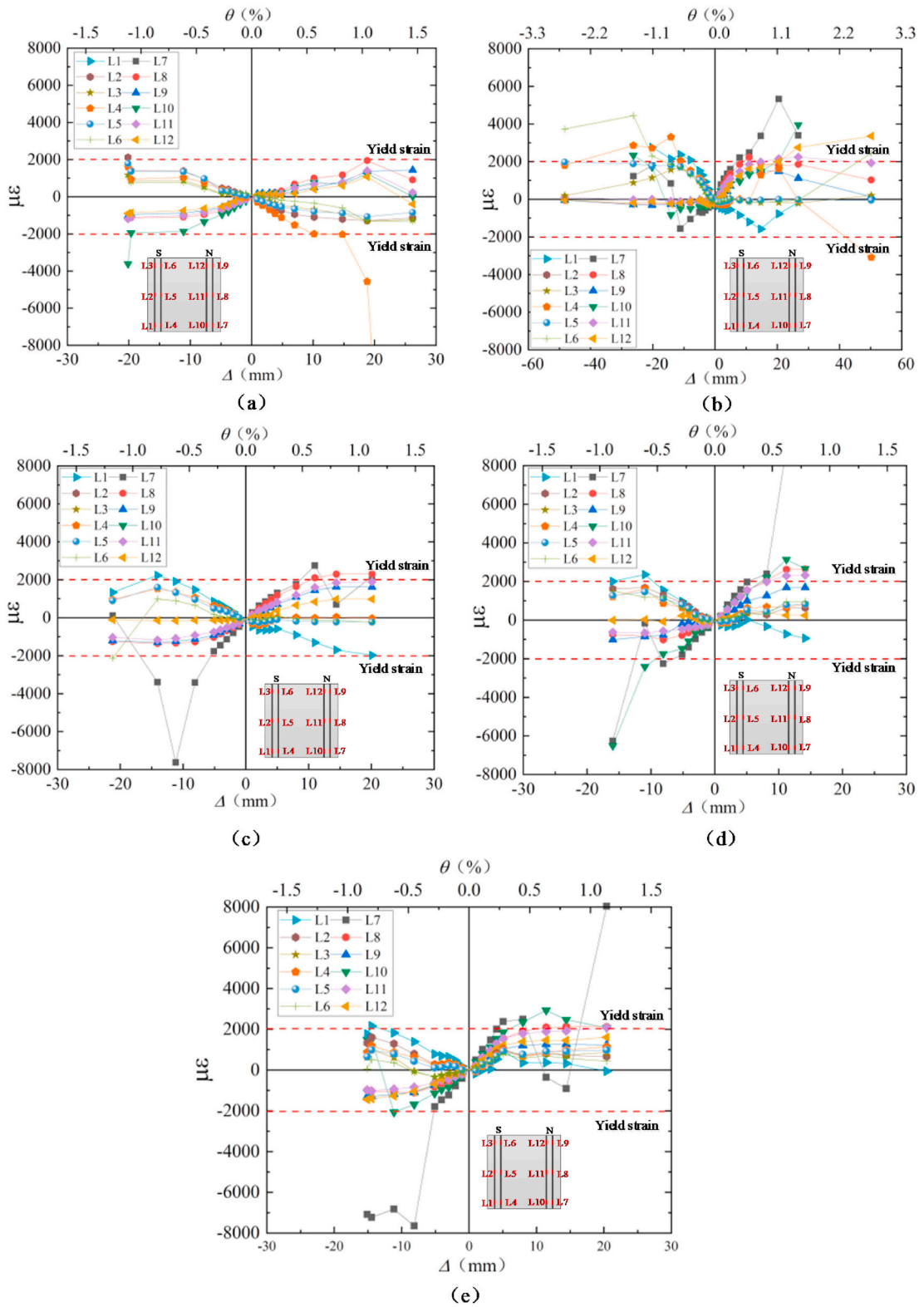


Fig. 14. Strains of boundary longitudinal reinforcement: (a) SW10-C-3; (b) SW10-T-1; (c) SW10-TC-1/3; (d) SW10-TC-2/3; (e) SW10-TC-3/3.

strains, in comparison to the control specimen SW10-C-3, the TC specimens exhibited an early compressive yielding under the compression-shear state. This could be one of the main reasons for the reduced compression-shear strength of the TC specimens compared to SW10-C-3.

3.7. Discussion on failure mechanism of TC specimens

Since this study mainly focuses on the shear performance of shear walls under alternating axial loads, the specimens were designed with a relatively high longitudinal reinforcement ratio to avoid flexural failure. All three TC specimens first reached peak shear loads under compression-shear state and eventually failed in this state. The target axial compressive load under compression-shear state for the TC specimens was the same. Therefore, it can be inferred that the different levels of damage caused by different target axial tensile loads in the tension-shear state resulted in different failure surfaces (Fig. 8 (c)–(e)) and shear capacities (Fig. 11 (b)) under compression-shear conditions. The greater the target axial tensile load in the tension-shear state, the wider the crack width at the same lateral horizontal displacement Δ (Fig. 6(e)–(g), and (i)), and the greater the tensile strain in the boundary longitudinal reinforcement on the tension side of the TC specimens (Fig. 14 (c)–(e)). When the TC specimens reached their compression-shear capacity, the boundary longitudinal reinforcement on the compression side, which previously yielded in tension under the tension-shear state, exhibited residual strains that increased with the target axial tensile load. Consequently, the width of horizontal cracks at the bottom of the compression side under the peak compression-shear strength of the TC specimens increased with the target axial tensile load, as shown in Fig. 7(f)–(h), and (j). Only the specimen SW10-TC-1/3, with the lowest target axial tensile load, did not exhibit significant horizontal cracks in the compression zone. These horizontal cracks formed during the tension-shear state and could not close when approaching the compression-shear capacity, leading to a reduction in the effective compressive strength of the concrete in the compression zone of the TC specimens. This is likely one of the main reasons why the compression-shear capacity of TC shear walls decreased with increasing target axial tensile load. As the lateral displacement continued to increase, the crack width kept growing. In specimen SW10-TC-3/3, the critical diagonal crack formed under compression-shear state combined with the horizontal cracks generated under tension-shear state, creating a failure surface through the cross-section of the specimen, as shown in Fig. 7 (i), leading to its ultimate failure.

The tension-shear capacity of the TC specimens also decreased with increasing target axial tensile load, and the reduction was more significant than that of the compression-shear capacity. As seen in Fig. 7(e)–(g), and (i), as the target axial tensile load increased, the widths of the main diagonal cracks at peak shear load increased, and the angles between these diagonal cracks and the horizontal plane decreased. This led to a reduction in the shear force carried by the aggregate interlock mechanism along the diagonal cracks and a decrease in the number of horizontal stirrups intersecting the diagonal cracks, together reducing the shear capacity of the TC shear walls.

4. Evaluation and modification of shear strength models for RC shear walls

To more comprehensively evaluate whether the shear models in existing design codes effectively reflect the impact of axial tensile load on the shear capacity of RC shear walls, 25 specimens under tension-shear (TS) loading and 8 specimens subjected to alternating tension-shear and compression-shear (TC) loading were collected. These collected tests, together with the tests conducted in this study, form an evaluation database (Table 5), where the shear walls are reported to fail in shear or shear-sliding. Additionally, a shear strength model for RC walls under axial tension proposed by Ding et al. [42] was also used for comparison with code models.

4.1. Shear strength models for RC shear walls

The shear strength equation for RC shear walls in the ACI 318-19 [40] code considers the shear resistance of concrete and horizontal distributed reinforcement, taking into account the influence of the axial load N .

$$V_{ACI} = \left(\alpha_c \sqrt{f'_c} + \rho_h f_{yh} \right) A_w \leq 0.66 \sqrt{f'_c} A_w \quad (3)$$

where V_{ACI} is the nominal shear strength predicted by ACI 318-19; A_w represents the area of the shear wall's web, calculated as the product of the web thickness b_w and the length of the entire wall l_w ; f_{yh} and ρ_h denote the yield strength and reinforcement ratio of horizontal distributed reinforcement, respectively; the concrete cylinder compressive strength f'_c is taken as the measured value in the test. The coefficient α_c varies with axial loads. For axial compressive load (negative values of N), when $h_w/l_w \leq 1.5$, $\alpha_c = 0.25$; when $h_w/l_w \geq 2.0$, $\alpha_c = 0.17$; and for $1.5 < h_w/l_w < 2.0$, α_c is obtained through linear interpolation; where h_w represents the height of the shear wall. When the axial load N is tension (positive values of N), α_c is calculated according to the following expression:

$$\alpha_c = 0.17 \left(1 - 0.29 \frac{N}{A_g} \right) \geq 0 \quad (4)$$

where A_g is gross area of the concrete section.

The shear strength, V_{JGJ} , for RC shear walls under earthquake in the Chinese code JGJ 3–2010 [41] is as follows:

$$V_{JGJ} = \frac{1}{\lambda - 0.5} \left(0.4 f_t b_w d_w - 0.1 N \frac{A_w}{A_g} \right) + 0.8 \rho_h f_{yh} b_w d_w \quad (5)$$

where λ represents the shear span-to-depth ratio, with respective upper and lower limits of 2.2 and 1.5, and it is taken as 2.0 for the

Table 5
Test database of RC shear walls subjected to axial tension.

Type	Authors and Reference	Specimen No.	$h \times b_w$	a/d_w	ρ_{be}	ρ_h	ρ_v	f_c'	N_t	N_c	n_t	n_s	V_{tt}	V_{tc}	Loading method
			mm ²		%	%	%	MPa	kN	kN			kN	kN	
1	Wang et al. [31]	SW-1	1000 × 120	1.57	10.9 %	0.47 %	0.84 %	37.1	0	–	0.00	0.00	603	–	TS
2		SW-2		1.57	10.9 %	0.47 %	0.84 %	37.1	176	–	0.39	0.08	543	–	TS
3		SW-3		1.57	10.9 %	0.47 %	0.84 %	37.1	380	–	0.83	0.18	436	–	TS
4		SW-4		1.57	10.9 %	0.47 %	0.84 %	37.1	578	–	1.27	0.27	427	–	TS
5	Ren et al. [32]	RCW17T100	800 × 120	1.61	4.7 %	0.39 %	0.59 %	66.2	157	–	0.34	0.22	231	–	TS
6		RCW17T150		1.61	4.7 %	0.39 %	0.59 %	60.8	235	–	0.52	0.33	203	–	TS
7		RCW25T000		1.61	7.9 %	0.39 %	0.59 %	50.1	0	–	0.00	0.00	404	–	TS
8		RCW25T200		1.61	7.9 %	0.39 %	0.59 %	40.5	415	–	1.14	0.39	324	–	TS
9		RCW25T250		1.61	7.9 %	0.39 %	0.59 %	48.5	579	–	1.39	0.55	260	–	TS
10	Ji et al. [5,35]	SW1	1500 × 180	1.22	5.6 %	0.37 %	0.58 %	49.7	617	–	0.52	0.25	960	–	TS
11		SW2		1.22	5.6 %	0.37 %	0.58 %	50.1	1030	–	0.86	0.41	823	–	TS
12		SW3		1.22	5.6 %	0.37 %	0.58 %	50.2	1716	–	1.42	0.69	568	–	TS
13		SW6		1.22	5.6 %	0.37 %	0.58 %	43.7	0	–	0.00	0.00	1173	–	TS
14	Nie et al. [6]	MSW1	1700 × 150	1.67	3.8 %	0.37 %	0.58 %	24.5	582	–	0.86	0.20	749	–	TS
15		T00		1.14	7.5 %	0.38 %	0.38 %	49.1	0	–	0.00	0.00	1507	–	TS
16		T30		1.14	7.5 %	0.38 %	0.38 %	49.1	776	–	0.70	0.28	1154	–	TS
17		T40		1.14	7.5 %	0.38 %	0.38 %	49.1	1034	–	0.93	0.37	1105	–	TS
18	Yao et al. [36]	T50	800 × 150	1.14	7.5 %	0.38 %	0.38 %	49.1	1293	–	1.16	0.46	1008	–	TS
19		W1		0.97	3.7 %	0.38 %	1.05 %	46.3	382	–	0.78	0.34	499	–	TS
20		W2		0.97	5.0 %	0.38 %	2.05 %	46.3	696	–	1.34	0.41	605	–	TS
21		W3		0.97	5.0 %	0.38 %	2.05 %	43.6	1044	–	2.10	0.62	517	–	TS
22	Wei et al. [37]	W4	1000 × 150	0.54	1.4 %	1.16 %	1.16 %	29.4	525	–	1.25	0.63	696	–	TS
23		W11		0.54	1.4 %	0.74 %	1.16 %	29.4	525	–	1.25	0.63	520	–	TS
24		W13		0.54	1.4 %	1.67 %	1.16 %	28.0	525	–	1.30	0.63	890	–	TS
25	Ren et al. [38]	RCW30T200	800 × 120	1.61	9.7 %	0.39 %	0.59 %	47.7	582	1810	1.38	0.46	364	758	TC
26		RCW30T400		1.61	9.7 %	0.39 %	0.59 %	44.9	1163	1810	2.88	0.92	249	470	TC
27	Huang et al. [39]	SW1	1000 × 150	1.11	5.09 %	0.38 %	0.56 %	36.9	569	1082	1.08	0.35	564	893	TC
28		SW2		1.11	5.09 %	0.38 %	0.56 %	36.9	1137	1650	2.15	0.70	388	915	TC
29		SW3		1.11	5.09 %	0.38 %	0.56 %	36.9	1137	1650	2.15	0.70	445	893	TC
30	This study	SW10-T-1	1400 × 150	2.16	12.5 %	0.38 %	0.38 %	35.1	700	–	0.91	0.19	685	–	TS
31		SW10-TC-1/3		2.16	12.5 %	0.38 %	0.38 %	35.1	700	2100	0.91	0.19	685	1039	TC
32		SW10-TC-2/3		2.16	12.5 %	0.38 %	0.38 %	33.4	1400	2100	1.89	0.39	512	942	TC
33		SW10-TC-3/3		2.16	12.5 %	0.38 %	0.38 %	32.5	2100	2100	2.89	0.58	360	898	TC

Notes: b_w and h are the web thickness and height of the wall cross-section, respectively; a/d_w represent shear span-to-effective depth ratio; ρ_{be} represent the reinforcement ratio of boundary element; ρ_h , ρ_v represent horizontal and vertical distributed reinforcement ratios, respectively; n_s represent axial tension ratio of vertical rebars, calculated as $N_t/(A_{sv}f_{yv})$, where A_{sv} and f_{yv} respectively represent the area and yield strength of vertical rebars (including the boundary longitudinal bars and the vertical distributed bars); V_{tt} , V_{tc} represent measured tensile and compressive peak shear loads, respectively.

specimens in this test; f_t stands for the concrete tensile strength, its value converted from f'_c based on a simplified method proposed by Reineck et al. [45].

Ding et al. [42] proposed a simplified model (Eqs. (6)–(9)) for the shear capacity of RC shear walls under tension-shear state, which is a simplification of a mechanics-based Cracking strut-and-tie model [46–48]. The shear model by Ding et al. considers the effects of horizontal distributed bars, concrete strength, and size effect on the shear strength through an effective coefficient for struts β_s . The effects of axial force N (tensile force as positive and compressive force as negative) and vertical reinforcement (including boundary longitudinal bars and vertical distributed bars) are accounted for through the width of the compression strut (determined by the compression zone height c at the bottom cross-section of walls). Additionally, the model takes the flange effect into account by using the equivalent wall width b_e .

$$V_{Ding} = \beta_s f'_c A_{str} \sin \theta = \beta_s f'_c c b_e \sin \theta \quad (6)$$

$$\beta_s = 0.5(1 + 100\rho_h)^{0.8} \left(\frac{500}{d_w}\right)^{0.2} \left(\frac{30}{f'_c}\right)^{0.5} \leq 0.85 \left(1 - \frac{f'_c}{250}\right) \quad (7)$$

$$\left(\frac{c}{d_w}\right)^2 + \left[1.5 \frac{h_f}{d_w} \left(\frac{b_f}{b_w} - 1\right) + 1.5 \frac{N}{b_w d_w f'_c} + 600 \frac{\rho_b + \rho_v}{f'_c}\right] \frac{c}{d_w} - 600 \frac{\rho_b + 0.5\rho_v}{f'_c} = 0 \quad (8)$$

$$b_e = b_w \left[1 + 0.5 \frac{h_f}{c} \left(\frac{b_f}{b_w} - 1\right)\right] \quad (9)$$

where V_{Ding} is the shear strength predicted by the model by Ding et al., A_{str} is the cross-sectional area of the compression strut; θ is the angle between the diagonal strut and the longitudinal reinforcement; h_f and b_f represent the thickness and width of the flange, respectively; ρ_b represents the reinforcement ratio of boundary longitudinal bars on one side; and ρ_v is the reinforcement ratio of vertical distributed bars.

4.2. Evaluation and modification of shear models

The tension-shear capacities V_{tt} of the specimens in the database were used to evaluate the shear models by ACI 318-19, JGJ 3–2010, and Ding et al. Their evaluation results are shown in Fig. 15, the average values of tested-to-predicted shear capacity ratios were 1.92, 1.70, and 1.12, respectively, with coefficients of variation (COVs) of 0.50, 0.38, and 0.19. This indicates that the shear model by Ding et al. predicts the tension-shear capacity of RC shear walls more accurately, whereas the shear models in ACI 318-19 and JGJ 3–2010 show excessive variability in their predictions.

Fig. 15 also distinguishes between TC specimens and TS specimens. It can be seen that both ACI 318-19 and JGJ 3–2010 do not consistently reflect the effect of the target axial tensile load (represented by axial tension ratio of vertical rebars n_s here) on the tension-shear strength of the two types of specimens. For TS specimens, the tested-to-predicted shear capacity ratios increase with n_s (Fig. 15 (a) and (b)), indicating that ACI 318-19 and JGJ 3–2010 may overestimate the adverse effects of axial tension on shear capacity. In contrast, the shear model by Ding et al. shows no significant variation trend with increasing n_s for both TC and TS specimens, suggesting that it better reflects the influence of axial tensile load on the tension-shear capacity of both types of specimens.

Fig. 16 shows the evaluation results of the shear models by ACI 318-19, JGJ 3–2010, and Ding et al. based on the compression-shear capacities of the TC specimens in the database. It can be observed that the tested-to-predicted shear capacity ratios for all three models shows a decreasing trend as n_s increases, with a similar rate of decline. This result is due to the fact that none of the three models consider the effect of alternating axial loads on the compression-shear capacity of shear walls.

To account for the adverse effects of alternating axial loads on the compression-shear capacity of shear walls, a reduction coefficient α was proposed based on the fitting of the test results of the TC specimens, as shown in Equation (10). By multiplying the predicted values of the shear models by this factor, the effect of alternating axial loads on the compression-shear capacity of RC shear walls can be considered. Since in most cases $n_s \leq 1$, meaning that the axial tensile force does not exceed the force required for the full yielding of vertical reinforcement, the minimum value of the reduction factor α is set to 0.75.

$$\alpha = 1 - 0.25n_s \geq 0.75 \quad (10)$$

The evaluation results of the three shear models after considering the reduction factor α are shown in Fig. 17. It can be observed that with increasing n_s , the tested-to-predicted shear capacity ratios for each shear model do not show a significant increasing or decreasing trend. This indicates that the shear models, with the reduction factor α taken into account, are able to adequately reflect the impact of alternating axial loads on the compression-shear capacity.

5. Summary and conclusions

- 1) In this study, cyclic tests were conducted on five large-scale shear wall specimens to investigate the influence of alternating axial tensile and compressive loads (alternating axial loads) on the seismic and shear performance of RC shear walls. The tests synchronized axial loads with lateral displacements, simulating the alternating tension-shear (-bending) and compression-shear (-bending) states of bottom wall piers in coupled shear wall structures.

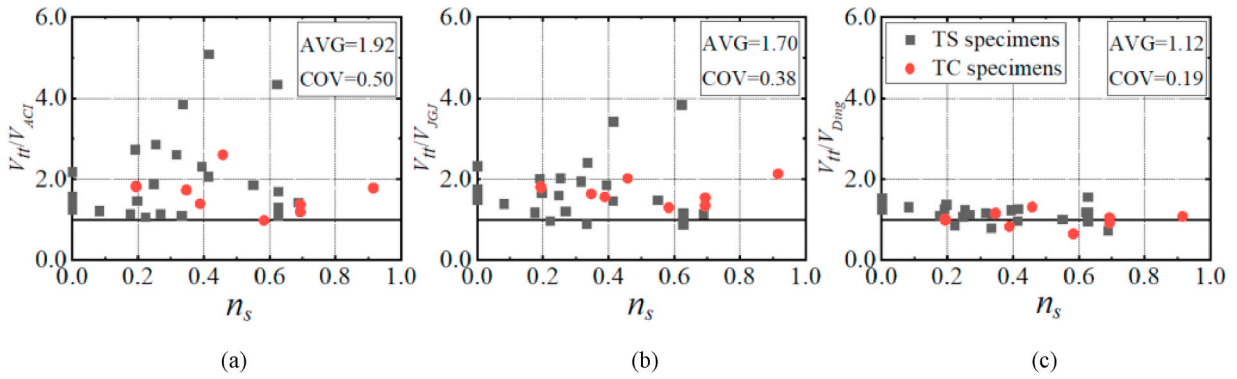


Fig. 15. Evaluation of tension-shear strength predicted by shear models of (a) ACI 318-19, (b) JGJ 3–2010, and (c) Ding et al.

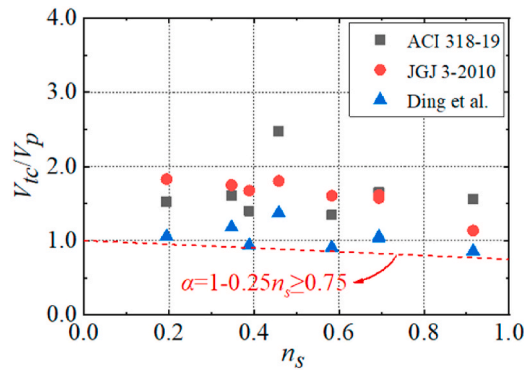


Fig. 16. Evaluation of compression-shear strength predicted by shear models.

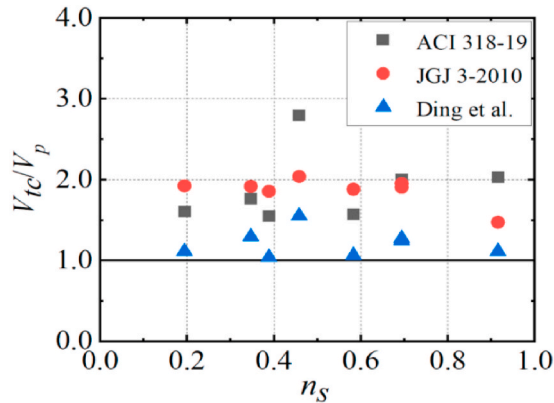


Fig. 17. Evaluation of compression-shear strength provided by modified shear model.

- 2) The crack patterns and failure characteristics of the TC specimens, which subjected to alternating axial loads, exhibited significant asymmetry. As the target axial tensile load increased, both the tensile-shear and compressive-shear strength decreased, with a more significant reduction observed in the former. Compared to the control specimens, when the maximum nominal tensile stress reached $0.3f_b$, the tension-shear and compression-shear capacities of SW10-TC-3/3 were reduced by 44.7 % and 19.4 %, respectively.
- 3) Compared to the tension-shear control specimen SW10-T-1, the ductility of the TC specimens significantly decreased in the tension-shear state. This resulted in a substantially lower energy dissipation capacity of the TC specimens compared to SW10-T-1, approaching that of the compression-shear control specimen.
- 4) Based on the tests conducted in this study and the collected existing tests, the shear capacity formulas for shear walls in the current codes ACI 318-19 and JGJ 3–2010 were evaluated and compared with a shear model previously proposed by the authors. The

results show that the authors' model predicts the tension-shear capacity of shear walls with a higher accuracy, exhibiting an average ratio of tested-to-predicted values of 1.12 and a coefficient of variation of 0.19. Furthermore, these models do not account for the effect of alternating axial loads on the compression-shear capacity of shear walls. Therefore, based on the fitting of experimental results, a coefficient was proposed to consider the shear capacity reduction caused by alternating axial loads.

CRedit authorship contribution statement

Ya-Bo Ding: Writing – original draft, Visualization, Software, Investigation, Formal analysis, Data curation. **Hui Chen:** Writing – review & editing, Resources, Project administration, Methodology, Funding acquisition. **Wei-Jian Yi:** Writing – review & editing, Supervision, Resources, Methodology, Conceptualization. **Zhongguo John Ma:** Writing – review & editing, Supervision. **Jing-Ming Sun:** Software, Resources, Investigation, Data curation. **Lei He:** Investigation. **Yun Zhou:** Writing – review & editing.

Declaration of competing interest

The authors declared that they have no conflicts of interest to this work.

Data availability

Data will be made available on request.

Acknowledgement

The authors would like to acknowledge the financial support provided for this work by the National Natural Science Foundation of China (No. 52008161), China Postdoctoral Science Foundation (No. 2021T140196), and Education Department of Hunan Province of China (No. 21C0367).

References

- [1] K.I. Christidis, D. Karagiannaki, Evaluation of flexural and shear deformations in medium rise RC shear walls, *J. Build. Eng.* 42 (2021) 102470.
- [2] K. Liang, R.K.L. Su, Experimental and theoretical study on seismic behavior of non-seismically designed shear walls with moderate shear span-to-length ratios, *J. Build. Eng.* 76 (2023) 107213.
- [3] A.H. Asjodi, K.M. Dolatshahi, A. Ebrahimkhanlou, Spatial analysis of damage evolution in cyclic-loaded reinforced concrete shear walls, *J. Build. Eng.* 49 (2022) 104032.
- [4] B. Wei, W.H. Wang, P. Wang, et al., Seismic responses of a high-speed railway (HSR) bridge and track simulation under longitudinal earthquakes, *J. Earthq. Eng.* 26 (9) (2022) 4449–4470.
- [5] X. Ji, X. Cheng, M. Xu, Coupled axial tension-shear behavior of reinforced concrete walls, *Eng. Struct.* 167 (2018) 132–142.
- [6] X. Nie, J.-J. Wang, M.-X. Tao, J.-S. Fan, Y. Mo, Z.-Y. Zhang, Experimental study of shear-critical reinforced-concrete shear walls under tension-bending shear-combined cyclic load, *J. Struct. Eng.* 146 (2020) 04020047.
- [7] F. Rojas, F. Naeim, M. Lew, L.D. Carpenter, N.F. Yousef, G.R. Saragoni, et al., Performance of tall buildings in Concepción during the 27 February 2010 moment magnitude 8.8 offshore Maule, Chile earthquake, *Struct. Des. Tall Special Build.* 20 (2011) 37–64.
- [8] C. Song, S. Pujol, A. Lepage, The collapse of the Alto Río building during the 27 February 2010 Maule, Chile, earthquake, *Earthq. Spectra* 28 (2012) 301–334.
- [9] Z.T. Deger, J.W. Wallace, Collapse assessment of the Alto Rio building in the 2010 Chile earthquake, *Earthq. Spectra* 31 (2015) 1397–1425.
- [10] P. Zhang, J.I. Restrepo, J.P. Conte, J. Ou, Nonlinear finite element modeling and response analysis of the collapsed Alto Rio building in the 2010 Chile Maule earthquake, *Struct. Des. Tall Special Build.* 26 (2017) e1364.
- [11] D. Ugalde, D. Lopez-Garcia, Analysis of the seismic capacity of Chilean residential RC shear wall buildings, *J. Build. Eng.* 31 (2020) 101369.
- [12] A. Aviram, D. Kelly, A. Birely, L. Lowes, D. Lehman, Disparate damage levels from the 2010 Maule, Chile earthquake in two similar reinforced concrete shear wall buildings. Proceedings of the 10th National Conference in Earthquake Engineering, Anchorage, AK, Earthquake Engineering Research Institute, 2014.
- [13] J. Moehle, in: 27 March 2010 Offshore Maule, Chile Earthquake, 2010. https://peer.berkeley.edu/sites/default/files/moehle_lfe_briefing_in_berkeley.pdf. UC Berkeley.
- [14] Y. Mo, J. Chan, Behavior of reinforced-concrete-framed shear walls, *Nucl. Eng. Des.* 166 (1996) 55–68.
- [15] F. Barda, Shear Strength of Low-Rise Walls with Boundary Elements, Lehigh University, 1972.
- [16] K. Orakcal, L.M. Massone, J.W. Wallace, Shear strength of lightly reinforced wall piers and spandrels, *ACI Struct. J.* 106 (2009) 455.
- [17] B. Luna, A. Whittaker, J. Rivera, in: Seismic Behavior of Low Aspect Ratio Reinforced Concrete Shear Walls, 2013.
- [18] D. Looi, R. Su, B. Cheng, H. Tsang, Effects of axial load on seismic performance of reinforced concrete walls with short shear span, *Eng. Struct.* 151 (2017) 312–326.
- [19] B.N. Luna, A.S. Whittaker, Peak strength of shear-critical reinforced concrete walls, *ACI Struct. J.* 116 (2) (2019) 257–266.
- [20] J.-H. Kim, H.-G. Park, Shear and shear-friction strengths of squat walls with flanges, *ACI Struct. J.* 117 (2020) 269–280.
- [21] M.-Y. Cheng, L.S. Wibowo, M.B. Giduquio, R.D. Lequesne, Strength and Deformation of Reinforced Concrete Squat Walls with High-Strength Materials, American Concrete Institute, 2021.
- [22] J.-H. Kim, H.-G. Park, Shear strength of flanged squat walls with 690 MPa reinforcing bars, *ACI Struct. J.* 119 (2022) 209–220.
- [23] G. Faraone, T.C. Hutchinson, R. Piccinin, J.F. Silva, Seismic performance of varying aspect ratio full-scale concrete walls, *ACI Struct. J.* 119 (2022).
- [24] C.K. Gulec, A.S. Whittaker, in: Performance-based Assessment and Design of Squat Reinforced Concrete Shear Walls: MCEER, 2009.
- [25] M. Del Carpio Ramos, A.S. Whittaker, C.K. Gulec, Predictive equations for the peak shear strength of low-aspect ratio reinforced concrete walls, *J. Earthq. Eng.* 16 (2012) 159–187.
- [26] S. Grammatikou, D. Biskinis, M.N. Fardis, Strength, deformation capacity and failure modes of RC walls under cyclic loading, *Bull. Earthq. Eng.* 13 (2015) 3277–3300.
- [27] C.L. Ning, B. Li, Probabilistic development of shear strength model for reinforced concrete squat walls, *Earthq. Eng. Struct. Dynam.* 46 (2017) 877–897.
- [28] M.L. Moretti, S. Kono, T. Obara, On the shear strength of reinforced concrete walls, *ACI Struct. J.* 117 (2020).
- [29] Z.T. Deger, C. Basdogan, Empirical equations for shear strength of conventional reinforced concrete shear walls, *ACI Struct. J.* 118 (2021) 61–71.
- [30] P. Chetchoisak, W. Chomchaipol, J. Teerawong, S. Shaingchin, Strut-and-tie model for predicting shear strength of squat shear walls under earthquake loads, *Eng. Struct.* 256 (2022) 114042.
- [31] T. Wang, T. Lai, H. Zhao, H. Lin, Y. Wang, Tensile-shear mechanical performance test of reinforced concrete shear wall, *Building Structure* 47 (2) (2017) 64–69 [In Chinese].

- [32] C. Ren, C. Xiao, P. Xu, Experimental study on tension-shear performance of reinforced concrete shear wall, *China Civ. Eng. J.* 51 (4) (2018) 20–33 [In Chinese].
- [33] Y. Xie, Experimental Study on Seismic Behaviour of Low-Rise Reinforced Concrete Shear Walls, South China University of Technology, Guangzhou, 2018. B.S. Dissertation [In Chinese].
- [34] X. Cheng, X. Ji, R.S. Henry, M. Xu, Coupled axial tension-flexure behavior of slender reinforced concrete walls, *Eng. Struct.* 188 (2019) 261–276.
- [35] X. Ji, M. Xu, X. Cheng, Z. Miao, Experimental study on axial tension-flexure-shearbehavior of moderate-aspect-ratio RC shear walls, *J. Build. Struct.* 42 (2021) 90–101 [In Chinese].
- [36] Z. Yao, X. Fang, H. Wei, Experimental study on shear behavior of reinforced concrete shear walls under eccentric tension, *J. Build. Struct.* 41 (4) (2020) 71–81 [In Chinese].
- [37] F. Wei, H. Chen, Y. Xie, Experimental study on seismic behavior of reinforced concrete shear walls with low shear span ratio, *J. Build. Eng.* 45 (2022) 103602.
- [38] C. Ren, C. Xiao, P. Xu, T. Chen, Low-cyclic repeated shear test on tension-compression variable axial force of reinforced concrete shear wall, *China Civ. Eng. J.* 51 (2018) 16–25 [In Chinese].
- [39] Huang Jian kang, Cheng Xiao wei, Li Yi et al. Experimental study on shear behavior of RC shear walls with small shear span ratio under tension compression variable axial force. *Eng. Mech.*,(S1):228-237 [in Chinese].
- [40] ACI Committee 318, Building Code Requirements for Structural Concrete (ACI 318-19): Commentary on Building Code Requirements for Structural Concrete (ACI 318R-19), American Concrete Institute, Farmington Hills, MI, 2019, p. 623.
- [41] JGJ3-2010, Technical Specification for Concrete Structures of Tall Building, China Architecture & Building Press Beijing, 2010 [In Chinese].
- [42] Y.B. Ding, H. Chen, J.M. Sun, et al., Lateral resistances of RC shear walls controlled by shear and sliding failure modes under axial tension, *Eng. Struct.* 318 (2024) 118786.
- [43] X. Lu, Y. Chen, Modeling of coupled shear walls and its experimental verification, *J. Struct. Eng.* 131 (2005) 75–84.
- [44] Y. Zhang, Z. Wang, Seismic behavior of reinforced concrete shear walls subjected to high axial loading, *ACI Struct. J.* 97 (2000) 739–750.
- [45] K.H. Reineck, D.A. Kuchma, K.S. Kim, S. Marx, Shear database for reinforced concrete members without shear reinforcement, *ACI Struct. J.* 100 (2003) 240–249.
- [46] W.J. Yi, Y. Li, H. Chen, et al., Shear strength evaluation of RC D-Regions based on Single-Panel Strut-and-Tie model, *Eng. Struct.* 265 (2022) 114500.
- [47] H. Chen, W.J. Yi, H.J. Hwang, Cracking strut-and-tie model for shear strength evaluation of reinforced concrete deep beams, *Eng. Struct.* 163 (2018) 396–408.
- [48] H. Chen, W.J. Yi, Z. John Ma, Shear-transfer mechanisms and strength modeling of RC continuous deep beams, *J. Struct. Eng.* 146 (11) (2020) 04020240.